Large-eddy simulation of a turbulent piloted methane/air diffusion flame (Sandia flame D)

H. Pitsch[a)]
Flow Physics and Computation Division, Department of Mechanical Engineering, Stanford University, Stanford, California 94040-3030

H. Steiner
Center for Turbulence Research, Department of Mechanical Engineering, Stanford University, Stanford, California 94040-3030

(Received 2 March 2000; accepted 16 June 2000)

The Lagrangian Flamelet Model is formulated as a combustion model for large-eddy simulations of turbulent jet diffusion flames. The model is applied in a large-eddy simulation of a piloted partially premixed methane/air diffusion flame (Sandia flame D). The results of the simulation are compared to experimental data of the mean and RMS of the axial velocity and the mixture fraction and the unconditional and conditional averages of temperature and various species mass fractions, including CO and NO. All quantities are in good agreement with the experiments. The results indicate in accordance with experimental findings that regions of high strain appear in layer like structures, which are directed inwards and tend to align with the reaction zone, where the turbulence is fully developed. The analysis of the conditional temperature and mass fractions reveals a strong influence of the partial premixing of the fuel. © *2000 American Institute of Physics.* [S1070-6631(00)50910-6]

I. INTRODUCTION

While numerical simulations of turbulent flows applying Reynolds averaging techniques solve equations for ensemble or time averaged mean quantities, Large-Eddy Simulations (LES) have the capability of resolving the major part of the turbulent kinetic energy of turbulent flows. Hence, only the influence of the small turbulent scales on the resolved field has to be modeled. Since, in addition, the small turbulent scales fulfill the common modeling assumption of isotropy much better than the large scales, a very high accuracy in predictions of the turbulent flow field can be achieved by using LES. This is particularly interesting for simulations of chemically reacting flows, where an accurate description of mixing is essential and very complex phenomena like turbulent transition and instabilities might be of great importance.

The success of LES in predictions of turbulent flows is due to the fact that the kinetic energy content of the turbulent motion decreases with increasing wave number. Thereby, the major part of the Reynolds stresses is resolved. In the modeling of the unresolved part it is still most important to represent the larger scales by a sub-grid scale model. However, since chemical reactions in nonpremixed combustion occur only by molecular mixing of fuel and oxidizer, which in practical applications occurs only on the dissipative turbulent scales, the combustion process occurs essentially at the smallest scales of the sub-filter level, and has to be modeled entirely. This also explains why sub-grid modeling techniques, which have successfully been used in predictions of sub-grid scale stresses and variances, might not necessarily be applicable in the modeling of the chemical source terms.

In recent years many studies have been devoted to *a priori* testing of the applicability of combustion models in LES.[1–7] Most of the proposed models have previously been used, or could very similarly be applied, in RANS calculations. Essentially, the proposed models can be divided into four categories: the direct method, the Linear-Eddy Model, the transported probability density function (pdf) method, and the conserved scalar method.

Similarly, as in RANS combustion models, the direct modeling of the spatially filtered chemical source terms is a very challenging problem. Different direct closure models have been proposed by DesJardin and Frankel.[1] They first show that modeling the reaction term by only using the resolved scales without a sub-grid model gives very poor agreement compared with DNS results. This has also been shown in many other studies, for instance by Colucci *et al.*[7] In addition they propose two different direct closure models based on the scale similarity assumption, which considerably improve the predictions, but are still not in good agreement with DNS data. The reason for this is obvious. The scale similarity assumption actually implies that the smallest resolved scales are statistically similar to the largest unresolved scales. This assumption seems to be very reasonable, but still, it does not assist in the modeling of the chemical source term. As mentioned earlier, in turbulent nonpremixed combustion, chemical reactions occur on the dissipative rather than the larger unresolved scales. This problem is inherent for all models, which estimate the reaction rates by only using the resolved scales and it explains why the com-

[a)]Author to whom correspondence should be addressed; Phone: (650) 725-6635; fax: (650) 725-7834; electronic mail: H.Pitsch@stanford.edu

bustion models applied in LES do not differ significantly from RANS combustion models.

The Linear-Eddy Model (LEM) has been proposed by Kerstein.[8] In this method scalar mixing is described in lines, the linear eddies, which are convectively transported with the mean flow. The governing one-dimensional equations include molecular transport as well as turbulent convection modeled by random flow field rearrangement events. This model has been formulated in the frame of LES by McMurtry *et al.*[9] In this implementation one or more linear eddies are solved for each computational control volume. The convective transport of the linear eddies is modeled by so called splicing events, which randomly exchange adjacent cell linear eddies based on the LES-resolved velocity field.

The transported compositional pdf method has been applied to turbulent reactive flows using RANS methods in many studies[10–12] and has also been extended to LES by using so called filtered density functions (FDF),[7,10,13] which are pdfs of the sub-grid scale scalar quantities.

The concept of sub-grid scale pdfs has also been adopted in the application of conserved scalar methods, which assume that the chemical state and thereby the species mass fractions, can be related to a conserved scalar, typically the mixture fraction in the case of nonpremixed combustion. Then, by presuming the sub-grid scale pdf of the mixture fraction $\widetilde{P}(Z)$, the filtered species mass fractions $\widetilde{Y}_i$ in each computational cell can be evaluated by

$$\widetilde{Y}_i = \int_{Z=0}^{1} Y_i(Z)\widetilde{P}(Z)dZ, \tag{1}$$

provided the functional dependence $Y_i(Z)$ is known. Here and in the following the tilde denotes density-weighted spatial filtering.

$\widetilde{P}(Z)$ is commonly assumed to follow a β-function distribution, parametrized by the first two moments of the mixture fraction. The filtered mixture fraction is determined by the solution of a transport equation; its sub-grid scale variance is typically given by a sub-grid scale model. The validity of the β-function representation of the pdf of the mixture fraction has been investigated by several authors using DNS data of nonpremixed reacting flows for constant and variable density.[1,3–5,14–16] The two main conclusions are that the β-function pdf provides an excellent estimate for the sub-grid scale mixture fraction distribution and that this estimate is even much better for LES than for RANS models. This is shown to be particularly true if the mixture fraction variance is taken from the DNS data, suggesting that the β-function as a model for the statistical distribution of the mixture fraction performs much better than the commonly used sub-grid scale models for the mixture fraction variance.

The mixture fraction variance can be determined by standard sub-grid scale modeling methods like the scale similarity model as proposed by Cook and Riley,[3] or by using a small scale equilibrium assumption and determining the remaining coefficient by the Dynamic Procedure following Pierce and Moin.[17] However, DesJardin and Frankel,[1] for instance, have shown that their modeling results do not differ if they use a δ-function instead of the β-function as sub-grid mixture fraction pdf in a conserved scalar approach. This conclusion depends certainly on the spatial resolution of the calculation and the turbulence intensity.

Different approaches have been used to specify the function $Y_i(Z)$ appearing in Eq. (1). Among these are the infinitely fast irreversible chemistry assumption,[17] the equilibrium assumption,[3] the conditional moment closure method,[6,18] and the steady laminar flamelet model.[4,5]

In the present study the Lagrangian Flamelet Model[19,20] is applied in a large-eddy simulation for a turbulent, piloted methane/air diffusion flame. The results are discussed and compared with experimental data by Refs. 21–23.

II. MATHEMATICAL MODEL

A. Large-eddy simulation

The set of equations solved in the current modeling study can be derived by applying a spatial, density-weighted filter to the continuity equation, the momentum equations, and the mixture fraction transport equation resulting in

$$\frac{\partial \overline{\rho}}{\partial t} + \boldsymbol{\nabla}\cdot(\overline{\rho}\widetilde{\boldsymbol{v}}) = 0, \tag{2}$$

$$\frac{\partial \overline{\rho}\widetilde{\boldsymbol{v}}}{\partial t} + \boldsymbol{\nabla}\cdot(\overline{\rho}\widetilde{\boldsymbol{v}}\widetilde{\boldsymbol{v}}) = -\boldsymbol{\nabla}\overline{p} + \boldsymbol{\nabla}\cdot\widetilde{\boldsymbol{\sigma}} - \boldsymbol{\nabla}\cdot(\overline{\rho}(\widetilde{\boldsymbol{v}\boldsymbol{v}} - \widetilde{\boldsymbol{v}}\widetilde{\boldsymbol{v}})), \tag{3}$$

$$\frac{\partial \overline{\rho}\widetilde{Z}}{\partial t} + \boldsymbol{\nabla}\cdot(\overline{\rho}\widetilde{\boldsymbol{v}}\widetilde{Z}) = \boldsymbol{\nabla}\cdot(\overline{\rho}\widetilde{D}_Z\boldsymbol{\nabla}Z) - \boldsymbol{\nabla}\cdot(\overline{\rho}(\widetilde{\boldsymbol{v}Z} - \widetilde{\boldsymbol{v}}\widetilde{Z})), \tag{4}$$

with

$$\widetilde{\boldsymbol{\sigma}} = \overline{\mu}((\boldsymbol{\nabla}\widetilde{\boldsymbol{v}}) + (\boldsymbol{\nabla}\widetilde{\boldsymbol{v}})^T) - \tfrac{2}{3}\overline{\mu}\boldsymbol{\nabla}\cdot\widetilde{\boldsymbol{v}}\,\boldsymbol{\delta}. \tag{5}$$

Here, ρ is the density, t the time, $\boldsymbol{v}$ the velocity vector, p the pressure, Z the mixture fraction, D_Z the molecular diffusion coefficient of the mixture fraction, $\boldsymbol{\delta}$ the unity tensor, and μ the dynamic viscosity.

The spatially filtered value $\overline{\phi}$ of a quantity ϕ is defined as

$$\overline{\phi} = \int_{\mathcal{D}} G(\boldsymbol{x}-\boldsymbol{x}')\phi(\boldsymbol{x}')d\boldsymbol{x}', \tag{6}$$

where $\mathcal{D}$ denotes the integration domain, $\boldsymbol{x}$ is the coordinate vector, and given the filter size $\boldsymbol{\Delta}$, the spatial filter function is defined as

$$G(\boldsymbol{x}-\boldsymbol{x}') = \begin{cases} 1, & \text{if } |\boldsymbol{x}-\boldsymbol{x}'| \leqslant \dfrac{\boldsymbol{\Delta}}{2}, \\ 0, & \text{otherwise.} \end{cases} \tag{7}$$

As mentioned earlier the tilde denotes the Favre filtered value, for any quantity ϕ given by $\widetilde{\phi} = \overline{\rho\phi}/\overline{\rho}$.

The unclosed terms in Eqs. (3) and (4) are expressed by using eddy viscosity type models, such that the sub-grid scale fluxes in the momentum equations and the mixture fraction transport equation are given by

$$\overline{\rho}(\widetilde{\boldsymbol{v}\boldsymbol{v}} - \widetilde{\boldsymbol{v}}\widetilde{\boldsymbol{v}}) = -2\overline{\rho}\nu_t\widetilde{\boldsymbol{S}}, \quad \widetilde{\boldsymbol{S}} = \tfrac{1}{2}((\boldsymbol{\nabla}\widetilde{\boldsymbol{v}}) + (\boldsymbol{\nabla}\widetilde{\boldsymbol{v}})^T) \tag{8}$$

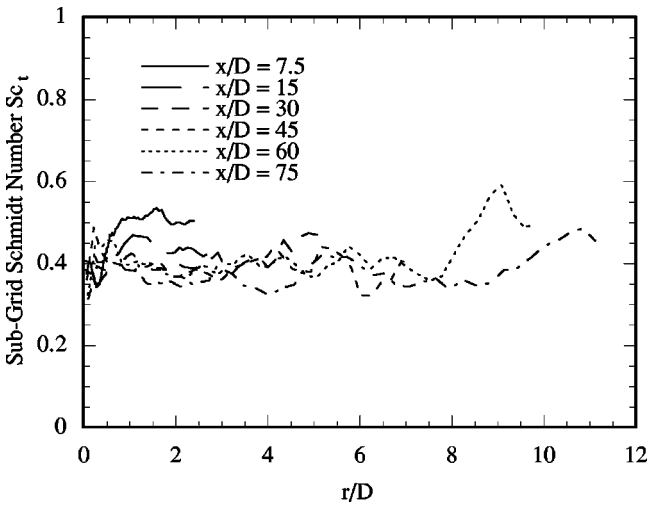

FIG. 1. Sub-grid scale Schmidt number of methane/air jet diffusion flame (Flame D) at different downstream positions.

and

$$\overline{\rho}(\widetilde{\boldsymbol{v}Z}-\widetilde{\boldsymbol{v}}\widetilde{Z})=-\overline{\rho}D_t\boldsymbol{\nabla}\widetilde{Z}, \tag{9}$$

where ν_t and D_t are the sub-grid kinematic eddy viscosity and eddy diffusivity, respectively.

The eddy viscosity ν_t is given by the Smagorinsky model as

$$\nu_t=C\Delta^2|\boldsymbol{S}|, \tag{10}$$

where following Moin *et al.*[24] the Smagorinsky constant C is determined by the Dynamic Model as a function of time and space. This procedure needs no model constants and assures that the turbulent fluxes vanish in the limit of a laminar flow.

The sub-grid diffusivity D_t is determined from

$$D_t=\nu_t/\mathrm{Sc}_t, \tag{11}$$

assuming a constant turbulent Schmidt number. In Reynolds averaged simulations the turbulent Schmidt number is commonly assumed to be equal to 0.7. However, in LES this value is different. An approximation for a constant sub-grid scale Schmidt number has been obtained by evaluating the sub-grid eddy viscosity ν_t and the sub-grid diffusivity D_t by applying the Dynamic Model. The sub-grid Schmidt number can then be determined from Eq. (11). The resulting time averaged sub-grid Schmidt number distribution for the flow configuration described below is shown in Fig. 1 at different downstream positions. The data clearly indicate that a constant value of $\mathrm{Sc}_t=0.4$ is a good approximation throughout the whole domain.

The sub-grid scale diffusivity D_t is computed as $D_t=\nu_t/\mathrm{Sc}_t$ assuming a constant turbulent Schmidt number $\mathrm{Sc}_t=0.4$. This value has been found to be appropriate from calculations, where D_t has also been determined by the Dynamic Model.

B. The Lagrangian Flamelet Model

The Lagrangian Flamelet Model (LFM) is used in this study to describe the turbulence–chemistry interactions. This approach has successfully been applied in RANS calculations of turbulent jet diffusion flames.[19,20] The model follows the conserved scalar approach, which has briefly been described in the Introduction, and uses the flamelet ideas.[25,26] Here however, the function $Y_i(Z)$ is determined by the solution of the unsteady rather than the steady flamelets equations.

The unsteady flamelet equations for the species mass fractions Y_i and the temperature T can be written as

$$\rho\frac{\partial Y_i}{\partial\tau}-\rho\frac{\chi}{2}\frac{\partial^2 Y_i}{\partial Z^2}-\dot{m}_i=0, \tag{12}$$

$$\rho\frac{\partial T}{\partial\tau}-\rho\frac{\chi}{2}\left(\frac{\partial^2 T}{\partial Z^2}+\frac{1}{c_p}\frac{\partial c_p}{\partial Z}\frac{\partial T}{\partial Z}\right)+\frac{1}{c_p}\left(\sum_{k=1}^{N}h_k\dot{m}_k+\dot{q}_R'''-\mathcal{H}\right)=0. \tag{13}$$

Here τ is a Lagrangian type flamelet time, h_i and $\dot{m}_i$ are the specific enthalpy and the chemical production rate per unit volume of species i, respectively, c_p is the constant pressure specific heat capacity, and the scalar dissipation rate χ has been introduced as

$$\chi=2D_Z\boldsymbol{\nabla}Z\cdot\boldsymbol{\nabla}Z. \tag{14}$$

D_Z is the diffusion coefficient of the mixture fraction and $\mathcal{H}$ accounts for the enthalpy flux by mass diffusion. The exact form for this term depends on the particular diffusion model and is given in Ref. 27 for the present work. In Eqs. (12) and (13) the Lewis numbers of all chemical species have been assumed to be unity. This assumption is discussed in great detail in Ref. 20, where it has been argued that in turbulent combustion only a thin region around the reaction zone is governed by molecular transport, whereas turbulent transport is predominant in the outer inert mixing region, which implies unity Lewis numbers. Numerical simulations have been performed for the present configuration assuming nonunity Lewis numbers. The results show that Lewis number effects indeed cannot explain the remaining discrepancies to the experimental data discussed below. These simulations show that the temperature is only influenced in the lean part of the flame. Of the major species only molecular hydrogen reveals changes on the rich side, which lead to an even stronger overprediction than the unity Lewis number results.

The radiation heat loss term $\dot{q}_R'''$ is represented by using an optically thin gray gas approximation as given by Smith *et al.*[28] This model provides some basic features of the radiation process, for example, that the heat loss essentially occurs at the highest temperature and that the radiation process is slow compared to other physical time scales of the problem, which has been discussed in detail in Ref. 19. The validity of the model has been assessed by comparing the predicted with the measured conditionally averaged temperatures at $x/D=60$ and $x/D=75$, which are in very good agreement. In contrast, calculations which neglect the influence of radiation overestimate the temperature at $x/D=75$ by approximately 100 K.

The consideration of the time dependence certainly adds some complexity to the problem, but it has been shown that

it is essential to consider the unsteadiness, if for instance radiation cannot be neglected or NO formation is considered.[19]

Equations (12) and (13) can readily be solved and the solution used to provide the remaining unknown quantities such as the density and the temperature if the scalar dissipation is known as a function of the mixture fraction, and the flamelet time τ can be related to the physical space coordinates. These relations will be derived next.

The basic idea of the model is that flamelets are introduced at the inflow boundary. These flamelets then move downstream, essentially by convective transport. In the following, for all instantaneous scalar quantities ϕ, where ϕ stands for the temperature or the species mass fractions, only averages over planes of equal nozzle distance x, conditioned on the mixture fraction, will be considered. This implies that these conditional averages, here denoted as $\langle \phi | Z \rangle (x,t)$ depend only on one spatial coordinate, the axial nozzle distance x, and the time t. Hence, the flamelet solution needed in Eq. (1) can be parametrized as a function of x and t as $Y_i(Z,x,t)$, where x will be expressed by the flamelet time τ.

Since flamelets are actually associated with the reaction zone, which is located in the vicinity of the stoichiometric mixture, the instantaneous local velocity of a flamelet particle has to be associated with the velocity of a point on the surface of a stoichiometric mixture fraction. Following Gibson[29] the velocity of iso-surfaces of a conserved scalar has contributions from the mean velocity and from the diffusion of that scalar. Thereby, the velocity of the resolved mixture fraction iso-surfaces can be expressed as

$$\tilde{\boldsymbol{v}}_{\tilde{Z}}(\boldsymbol{x},t) = \tilde{\boldsymbol{v}}(\boldsymbol{x},t) - \frac{\boldsymbol{\nabla} \cdot (\overline{\rho}(D_Z + D_t) \boldsymbol{\nabla} \tilde{Z})}{\overline{\rho} |\boldsymbol{\nabla} \tilde{Z}|} \boldsymbol{i}_Z, \tag{15}$$

where $i_Z = \boldsymbol{\nabla} \tilde{Z} / |\boldsymbol{\nabla} \tilde{Z}|$ is the unit vector in the direction of the gradient of the resolved mixture fraction.

If Eq. (15) is multiplied by the unit direction vector $\boldsymbol{e}_x$, then conditionally averaged over planes of equal nozzle distance x, and written for $\tilde{Z} = Z_{\mathrm{st}}$, one obtains for the resolved axial velocity u of the stoichiometric mixture fraction surface,

$$\langle \tilde{u}_{\tilde{Z}} | \tilde{Z} = Z_{\mathrm{st}} \rangle (x,t) = \langle \tilde{u} | \tilde{Z} = Z_{\mathrm{st}} \rangle (x,t) - \left\langle \left(\frac{\boldsymbol{\nabla} \cdot (\overline{\rho}(D_Z + D_t) \boldsymbol{\nabla} \tilde{Z})}{\overline{\rho} |\boldsymbol{\nabla} \tilde{Z}|^2} \frac{\partial \tilde{Z}}{\partial x} \right) \middle| \tilde{Z} = Z_{\mathrm{st}} \right\rangle, \tag{16}$$

which will be written as $\langle \tilde{u}_{\tilde{Z}} | \tilde{Z}_{\mathrm{st}} \rangle$ in the following. Equation (16) can now be used to relate the Lagrangian type flamelet time τ to the flamelet location in physical space as

$$\tau = \int_0^x \frac{1}{\langle \tilde{u}_{\tilde{Z}} | \tilde{Z}_{\mathrm{st}} \rangle (x',t)} dx'. \tag{17}$$

The second term on the right hand side of Eq. (16) represents the axial component of the velocity of the stoichiometric surface caused by diffusion normal to this surface. Hence, this term is identical to zero, if the mixture fraction gradient vector $\boldsymbol{i}_Z$ is normal to the nozzle axis. This indeed is a good approximation for the time averaged mixture fraction field in turbulent jet diffusion flames. Since in the present formulation both the conditional averaging in Eq. (16) and also the integration in Eq. (17) introduce an average, the net effect of this term on the Lagrangian type flamelet time τ is also assumed to be small and is therefore neglected.

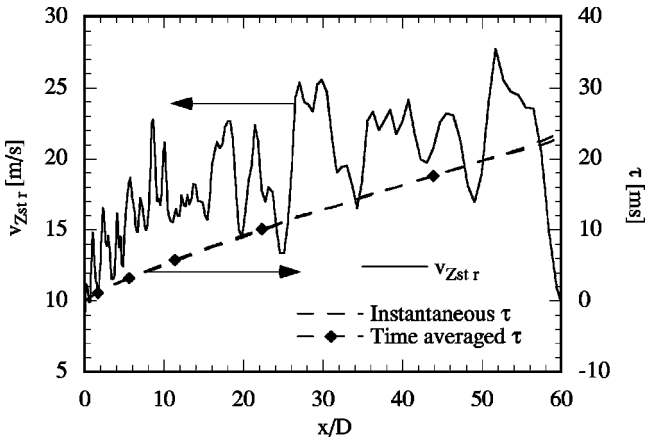

FIG. 2. Instantaneous velocity of the stoichiometric surface and instantaneous and time averaged Lagrangian type flamelet time as a function of the nozzle distance.

As an example, Fig. 2 shows one instantaneous realization of $\langle \tilde{u}_{\tilde{Z}} | \tilde{Z}_{\mathrm{st}} \rangle$ and the corresponding development of the Lagrangian type flamelet time τ as a function of the dimensionless nozzle distance x/D. It is very obvious that the velocity $\langle \tilde{u}_{\tilde{Z}} | \tilde{Z}_{\mathrm{st}} \rangle$ reveals strong turbulent fluctuations, whereas these do not appear in τ. The reason for this can be explained as follows. It is also obtained in Fig. 2 that after a transitional region at approximately $x/D = 10$, when the jet becomes self-similar, the mean value of $\langle \tilde{u}_{\tilde{Z}} | \tilde{Z}_{\mathrm{st}} \rangle$ hardly changes and seems to be around 20 m/s, independent of x/D. This independence of the axial nozzle distance can be shown analytically[30] and has also been found in experiments.[31] The integration in Eq. (17) can hence be interpreted as a time integration, which would, after normalization, yield the time averaged mean velocity at stoichiometric mixture. This in turn implies that the time average of τ should not be different from any instantaneous representation. Indeed, comparing the instantaneous representation of τ with the time averaged value, which is also given in Fig. 2, shows that these are almost identical.

Using Eqs. (12) and (17) the resolved mass fractions of chemical species $\widetilde{Y_i}$ are given by

$$\tilde{Y}_i(\boldsymbol{x},t) = \int_{Z=0}^{1} Y_i(Z,x,t) \tilde{P}(Z,\boldsymbol{x},t) dZ. \tag{18}$$

$\tilde{P}(Z,\boldsymbol{x},t)$ is presumed to follow a β-function, whose shape is determined by the mean and the sub-grid scale variance of the mixture fraction. Since no transport equation for the mixture fraction variance is solved, this value has to be modeled. Following Pierce and Moin[17] the sub-grid scale mixture fraction variance can be expressed as

$$\widetilde{\overline{\rho}\,Z''^2} = C_Z \Delta^2 \overline{\rho} |\nabla \widetilde{Z}|^2, \tag{19}$$

where the coefficient C_Z is determined using the Dynamic Procedure.

Similarly, the spatially filtered scalar dissipation rate, which will be needed in the following, is expressed in terms of the eddy diffusivity and the gradient of the resolved mixture fraction following Girimaji and Zhou[32] as

$$\widetilde{\chi} = 2(D_Z + D_t) \nabla \widetilde{Z} \cdot \nabla \widetilde{Z}, \tag{20}$$

where following Smooke[33] $D_Z \sim T^{1.7}$, which is evaluated with the mean temperature.

In Eqs. (12) and (13), the temporal development of the scalar dissipation rate is unknown and has to be related to the unconditional mean given by Eq. (20). A common approach is to presume the functional dependence of the scalar dissipation rate on the mixture fraction as $\langle \chi | Z \rangle (x,t) = \langle \chi_{st} \rangle \times (x,t) f(Z)$, where different analytic expressions for the function $f(Z)$ have been suggested.[19,25,34] Then, it is sufficient to determine the value conditioned on stoichiometric mixture. This can be achieved by using this expression in the equation for the filtered scalar dissipation rate $\widetilde{\chi}$, which can be written as

$$\widetilde{\chi}(\mathbf{x},t) = \int_{Z=0}^{1} \langle \chi | Z \rangle (x,t) \widetilde{P}(Z,\mathbf{x},t) dZ. \tag{21}$$

However, since in the present study a piloted flame is considered, the function $f(Z)$ cannot be represented by the commonly applied expressions, which will be demonstrated below.

In the present model, the conditional average of the scalar dissipation rate as a function of the axial distance from the nozzle $\langle \chi | Z \rangle (x,t)$ is computed by the inversion of the integral in Eq. (21), similar to the approach used by Bushe and Steiner[6] for the estimation of chemical source terms. The details of this model are described in Ref. 35, where also predictions for $\langle \chi | Z \rangle (x,t)$ close to the nozzle are presented and discussed. There, it is shown that the influence of the pilot flame on flame stabilization can be explained only by its influence on the conditional scalar dissipation rate.

It should be noted that this model also ensures that the actual flamelet does not necessarily extend over the whole mixture fraction space. This can be observed from the conditional mean scalar dissipation rate distributions at $x/D = 15$, 30, and 45, which are given in Fig. 3. At $x/D = 15$ the scalar dissipation rate still extends over the complete mixture fraction space. This has already changed at $x/D = 30$, where the maximum mixture fraction value with nonzero scalar dissipation rate has become smaller than unity. This continues in the downstream direction, such that at $x/D = 45$ the scalar dissipation rate is zero for $Z > 0.65$. In the calculations of the flamelets this region is still included. However, it can easily be seen from Eqs. (12) and (13) that for zero scalar dissipation rate, diffusive transport in mixture fraction space vanishes, resulting in localized homogeneous reactors at each value of Z, which are independent from each other.

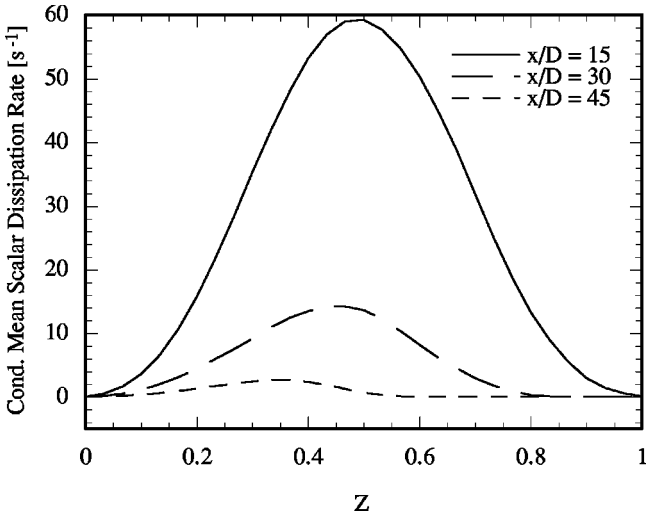

FIG. 3. Conditional mean scalar dissipation rate at different downstream locations.

In order to solve the unsteady flamelet equations, the scalar dissipation rate $\chi(Z,\tau,t)$ appearing in Eqs. (12) and (13), which can be written as $\chi(Z,x,t)$, has to be expressed in terms of the conditional mean scalar dissipation rate $\langle \chi | Z \rangle (x,t)$ determined from Eq. (21). The closure assumption here is that $\chi(Z,x,t)$ is given by the conditional mean scalar dissipation rate,

$$\chi(Z,x,t) = \langle \chi | Z \rangle (x,t), \tag{22}$$

which in turn implies that also the results obtained by solving the flamelet equations are conditional mean values.

In this model the solution of the flamelet equations $Y_i(Z,x,t)$ is still a function of the time t, because the Lagrangian type flamelet time $\tau(x,t)$ given by Eq. (17) and also the model for the scalar dissipation rate given by Eq. (22) have an implicit time dependence. However, as demonstrated in Fig. 2, the comparison of an arbitrary instantaneous representation of τ with its time averaged mean indicates that the time dependence of τ is very weak and will therefore be neglected. In order to simplify the model, the time dependence of the scalar dissipation rate is also neglected, which means that in the calculations presented below time averaged values are used for the scalar dissipation rate.

Note that this assumption still allows for turbulent fluctuations of the resolved mass fractions and temperature, because it only neglects the influence of fluctuations of the scalar dissipation rate on the chemistry. This assumption can be justified for nonpremixed combustion far from extinction as discussed by Kuznetsov and Sabel'nikov.[36] The reason for this is that for lower values of the scalar dissipation rate its influence on the mass fractions of the chemical species and the temperature is weak, as for instance shown in Ref. 27. The validity of this assumption is demonstrated in Ref. 35 by a comparison with calculations using the time dependent instantaneous conditional scalar dissipation rate.

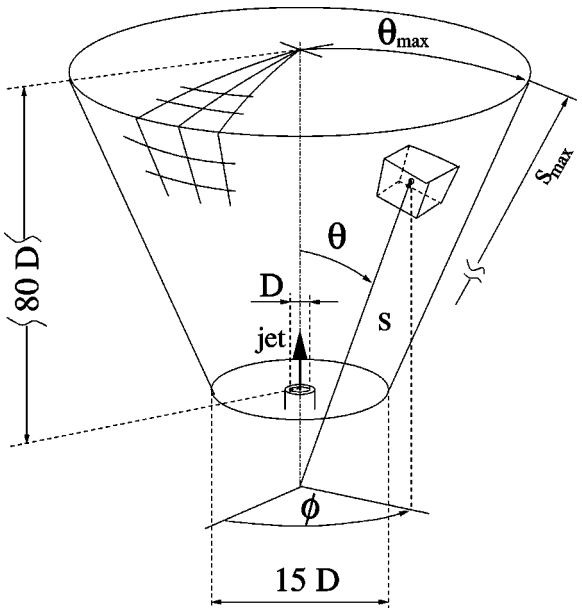

FIG. 4. Schematic representation of the coordinate system used in the simulation.

III. NUMERICAL PROCEDURE

A. Algorithm

The numerical computation of the flow was carried out with a second-order finite volume code, which has originally been developed for the DNS of nonreacting, low Mach number turbulent jets by Boersma *et al.*[37] The computational mesh is in spherical coordinates as shown in Fig. 4. It has 192 cells in the radial direction s, 110 points in the tangential direction Θ, and 48 points in the azimuthal direction ϕ.

The LES transport equations for momentum and the scalar Z as given by Eqs. (3) and (4) are advanced in time using a predictor–corrector-projection scheme following Najm *et al.*[38] The advancement of the numerical solution from time-level t^n to $t^{n+1}=t^n+\Delta t^n$ involves the following steps.

(1) The Adams–Bashford predictor-step:

$$(\widehat{\overline{\rho}\widetilde{u}_i})^*=(\widehat{\overline{\rho}\widetilde{u}_i})^n-\frac{\Delta t^n}{2}\left[\left(2+\frac{\Delta t^n}{\Delta t^{n-1}}\right)(\text{adv.}+\text{diff.})^n_{u_i}-\frac{\Delta t^n}{\Delta t^{n-1}}(\text{adv.}+\text{diff.})^{n-1}_{u_i}\right], \tag{23}$$

$$(\widetilde{\overline{\rho}\widetilde{Z}})^*=(\widetilde{\overline{\rho}\widetilde{Z}})^n-\frac{\Delta t^n}{2}\left[\left(2+\frac{\Delta t^n}{\Delta t^{n-1}}\right)(\text{adv.}+\text{diff.})^n_{Z}-\frac{\Delta t^n}{\Delta t^{n-1}}(\text{adv.}+\text{diff.})^{n-1}_{Z}\right], \tag{24}$$

yields the predictions denoted with the asterisk resulting from the advective and diffusive fluxes, here abbreviated as (adv.+diff.), which are given at the time-levels t^n and t^{n-1}. Even though for the sake of a simple notation it is not indicated in Eqs. (23) and (24) all diffusive terms, which involve derivatives with respect to ϕ, are treated implicitly. A TVD scheme is applied for the advection of the scalar Z to avoid spurious oscillations in the vicinity of strong gradients which occur particularly in the shear layer of the jet close to the nozzle exit, where large amounts of unmixed fuel meet the oxidizer from the co-flow.

(2) The predicted density $\overline{\rho}^*$ is obtained by

$$\widetilde{Z}^*=\frac{(\widetilde{\overline{\rho}\widetilde{Z}})^*}{\overline{\rho}^n}, \tag{25}$$

$$\frac{1}{\overline{\rho}^*}=\int_0^1\frac{1}{\rho(Z,s)}\widetilde{P}^*(Z,\boldsymbol{x},t)\,dZ, \tag{26}$$

integrating the pdf of the mixture fraction given as $\widetilde{P}^*(Z,\boldsymbol{x},t)=P(Z,\widetilde{Z}^*,\widetilde{Z''^2}^*)$. The density $\rho(Z,s)$ is given by the solution of the flamelet equations as described in the previous section. The sub-grid scale variance of the mixture fraction $\widetilde{Z''^2}^*$ is evaluated using $\widetilde{Z}^*$ in Eq. (19).

(3) Pressure correction: The corrected velocity field at the predictor level is computed as

$$(\widetilde{\overline{\rho}\widetilde{u}_i})^*=(\widehat{\overline{\rho}\widetilde{u}_i})^*-\Delta t^n\frac{\partial p^*}{\partial x_i}, \tag{27}$$

where the pressure gradient is obtained from the solution of the Poisson equation,

$$\left[\frac{\partial(\widehat{\overline{\rho}\widetilde{u}_i})^*}{\partial x_i}+\frac{\partial\overline{\rho}^*}{\partial t}\right]=\frac{1}{\Delta t^n}\frac{\partial^2 p^*}{\partial x_i\partial x_i}, \tag{28}$$

with the time derivative of the density being approximated by

$$\frac{\partial\overline{\rho}^*}{\partial t}\approx\frac{\left[\left(1+\frac{\Delta t^n}{\Delta t^{n-1}}\right)^2-1\right]\overline{\rho}^*-\left(1+\frac{\Delta t^n}{\Delta t^{n-1}}\right)^2\overline{\rho}^n+\overline{\rho}^{n-1}}{\Delta t^n\Delta t^{n-1}\left(1+\frac{\Delta t^n}{\Delta t^{n-1}}\right)}. \tag{29}$$

(4) The Adams–Molton corrector-step:

$$(\widehat{\overline{\rho}\widetilde{u}_i})^{n+1}=(\widehat{\overline{\rho}\widetilde{u}_i})^n-\frac{\Delta t^n}{2}[(\text{adv.}+\text{diff.})^n_{u_i}+(\text{adv.}+\text{diff.})^*_{u_i}], \tag{30}$$

$$(\widetilde{\overline{\rho}\widetilde{Z}})^{n+1}=(\widetilde{\overline{\rho}\widetilde{Z}})^n-\frac{\Delta t^n}{2}[(\text{adv.}+\text{diff.})^n_{Z}+(\text{adv.}+\text{diff.})^*_{Z}], \tag{31}$$

involves the advective and diffusive fluxes, (adv.+diff.)*, obtained with the predictor-step solution $\overline{\rho}^*$, $\widetilde{u}_i^*$, $\widetilde{Z}^*$.

(5) $\overline{\rho}^{n+1}$ is computed by

$$\widetilde{Z}^{n+1}=\frac{(\widetilde{\overline{\rho}\widetilde{Z}})^{n+1}}{\overline{\rho}^*}, \tag{32}$$

$$\frac{1}{\overline{\rho}^{n+1}}=\int_0^1\frac{1}{\rho(Z,r)}\widetilde{P}(Z,\boldsymbol{x},t)^{n+1}\,dZ. \tag{33}$$

(6) Pressure correction:

$$(\widetilde{\overline{\rho}\widetilde{u}_i})^{n+1}=(\widehat{\overline{\rho}\widetilde{u}_i})^{n+1}-\Delta t^n\frac{\partial p^{n+1}}{\partial x_i}, \tag{34}$$

with the pressure gradient obtained from the Poisson equation:

$$\left[\frac{\partial(\widetilde{\overline{\rho}}\widetilde{u}_i)^{n+1}}{\partial x_i}+\frac{\partial(\overline{\rho})^{n+1}}{\partial t}\right]=\frac{1}{\Delta t^n}\frac{\partial^2 p^{n+1}}{\partial x_i \partial x_i}. \tag{35}$$

B. Boundary conditions

At the inflow boundary all the required mean quantities are specified according to the experimental data given in Ref. 22 for the fuel jet, pilot, and co-flowing air stream. Velocity fluctuations are added to the measured mean profiles $u_{\mathrm{in},m}$ to mimic turbulent inflow conditions. The perturbed axial inflow velocity $\tilde{u}_{\mathrm{in}}$ is obtained by superimposing rotating helical and oscillating axisymmetric perturbations[39] on the mean profile as

$$\tilde{u}_{\mathrm{in}}(\Theta,t)=u_{\mathrm{in},m}+\sum_{i=1}^{6}\left[A_i\sin(\alpha_i+i\phi+\Psi_i t)\right]+\sum_{i=7}^{8}\left[A_i\sin(\Psi_i t)\right]. \tag{36}$$

The numerical values for α_i, which determine the phase shift of each helical mode in the azimuthal direction relative to $i\phi$, as well as the frequencies Ψ_i are randomly chosen. The coefficients A_i are specified to match the time averaged inflow velocity RMS $u'_{\mathrm{in},m}$ observed in the experiments. With the present velocity perturbation this is achieved by setting $A_i=0.5\cdot u'_{\mathrm{in},m}$ for all modes $i=1,\ldots,8$. Calculations have also been performed without the random velocity fluctuations resulting in only very slight changes in the flow field predictions.

Following Akselvoll and Moin[40] a convective boundary condition is used for the outflow boundary at $s=s_{\max}$ as

$$\frac{\partial\tilde{u}_i}{\partial t}+U_{\mathrm{con}}\frac{\partial\tilde{u}_i}{\partial s}=0. \tag{37}$$

Therein, the convection velocity U_{con} is the mean outflow velocity averaged over the azimuthal direction ϕ. The convective boundary condition convects vortical structures, which eventually approach the outflow boundary, out of the computational domain, thereby stabilizing the simulation. Although this approach introduces an error in elliptic problems, it can still be applied to flows of convective nature like free jets without disturbing the upstream solution.[37] However, the region very close to the outflow boundary has to be disregarded in the analysis of the numerical results.

A traction-free condition is used for the lateral boundary at $\Theta=\Theta_{\max}$.[41] This condition is given by

$$\boldsymbol{\sigma}\cdot\boldsymbol{n}=\mathbf{0}, \tag{38}$$

where $\boldsymbol{n}$ is the unit vector normal to the boundary. Unlike the no-slip or free-slip conditions it allows for a flux of ambient fluid across the lateral boundary. Thus, it is well-suited to capture the entrainment in a spreading jet.

C. Flamelet calculations

The unsteady flamelet calculations have been performed using the FLAMEMASTER code.[42] The chemical mechanism used for the results presented in the following is the GRI 2.11 mechanism,[43] which includes reactions among 48 chemical species. In order to reduce the computational time a reduced version of the mechanism has been developed, which consists of 29 global reactions. The reduced chemical scheme has been kept rather large in order to avoid numerical difficulties in the formulation of the steady state concentrations and to yield exactly the same results as the original mechanism. As an example, the maximum difference in the NO mass fraction calculated using the detailed and the reduced mechanism is approximately 0.4%.

It will be discussed below that the main differences in the comparison of predictions and experiments is in the onset of chemical reactions in the very rich premixed part of the configuration, which in the current predictions occurs too early. In order to investigate the influence of the chemical scheme on the computational results, unsteady flamelet calculations have been performed with different chemical mechanisms, including GRI 3.0[44] and recent mechanisms from other authors.[45–48] The predictions using the mechanism by Warnatz show large differences and a strong overprediction of the temperature in the rich part of the flame, because the mechanism predicts the onset of chemical reactions in that region even earlier. The results obtained by the remaining mechanisms show some differences in the mass fractions of individual species. But only for the NO mass fractions a stronger sensitivity to the individual chemical scheme is observed. The GRI 3.0 mechanism, for instance, leads to substantially higher NO mass fraction than GRI 2.11. However, the qualitative performance of all these chemical schemes is very similar.

IV. RESULTS AND DISCUSSION

The configuration used for the validation of the proposed models is a piloted methane/air jet diffusion flame (Sandia Flame D). The fuel is a 25/75% methane/air mixture. The fuel has been premixed with air in order to minimize the formation of polycyclic aromatic hydrocarbons and soot. The fuel nozzle has a diameter of $D=7.2$ mm and is enclosed by a broad pilot nozzle with a diameter of $D_{\mathrm{p}}=2.62D$ and an air-co-flow. In the experiments the pilot composition and temperature have been adjusted such that the pilot stream has the same equilibrium composition as a mixture of the main fuel and oxidizer with a mixture fraction of $Z=0.27$, which is slightly lean compared with a stoichiometric mixture fraction of $Z=0.35$. In the LES the pilot can thereby be represented by specifying the appropriate inlet mixture fraction. The fuel bulk velocity is 49.6 m/s, which leads to a fuel stream based Reynolds number of $\mathrm{Re}=22400$.

The flame has been experimentally investigated by Hassel *et al.*,[23] who provided data for the velocity field obtained by LDV measurements and by Barlow and Frank,[21,22] who performed Rayleigh measurements for the temperature, and Raman and LIF measurements to obtain mass fractions of chemical species and the mixture fraction.

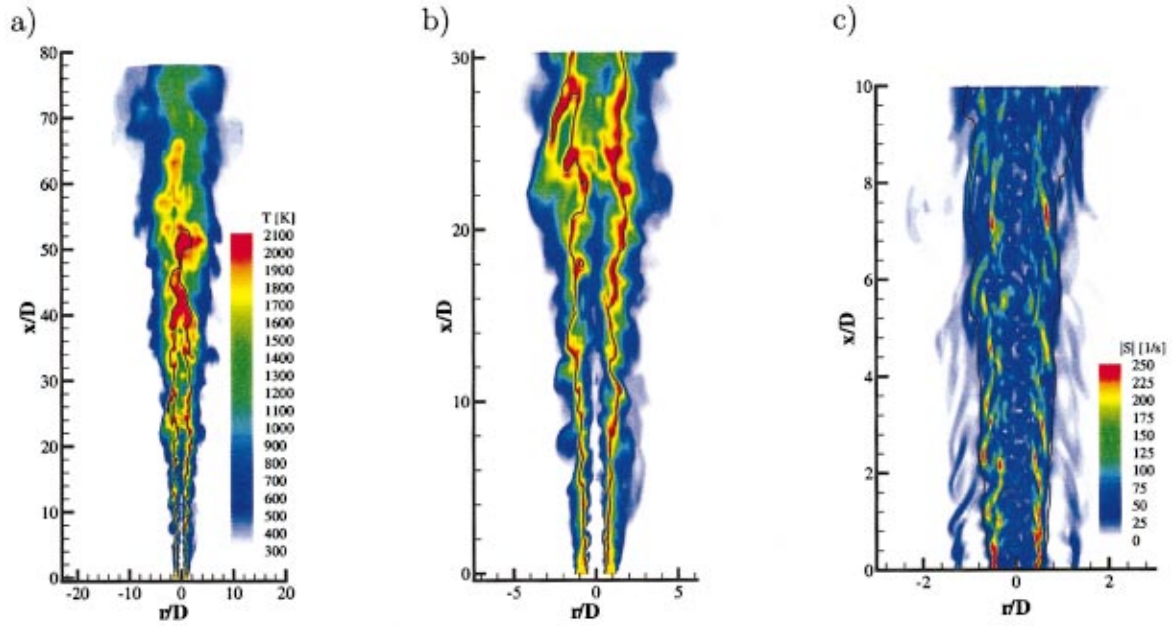

FIG. 5. (Color) Instantaneous temperature and strain rate distribution. The black line represents the contour of the stoichiometric mixture fraction.

In the remaining part of the paper, time averaged results from the simulation are discussed and compared with the experimental data. The averages have been obtained from the computational results by sampling over two flow-through times, where the flow-through time is defined as the time a particle traveling along the centerline would reside within the flow field. After a general discussion of the flame, the predictions of the flow field calculation, including velocity and mixture fraction field will be discussed. These results essentially serve as input quantities for the combustion model. Then, the predicted temperature and species mass fractions will be shown and compared with unconditionally and conditionally averaged experimental data.

A. General observations

Figure 5(a) shows an instantaneous temperature field of the computed jet and Fig. 5(b) gives an enlarged view of the near field region at the same instance. Also shown in these figures is the surface of the stoichiometric mixture, which indicates the location of the reaction zone. Figure 5(b) clearly shows the broad pilot flame. It is also interesting to

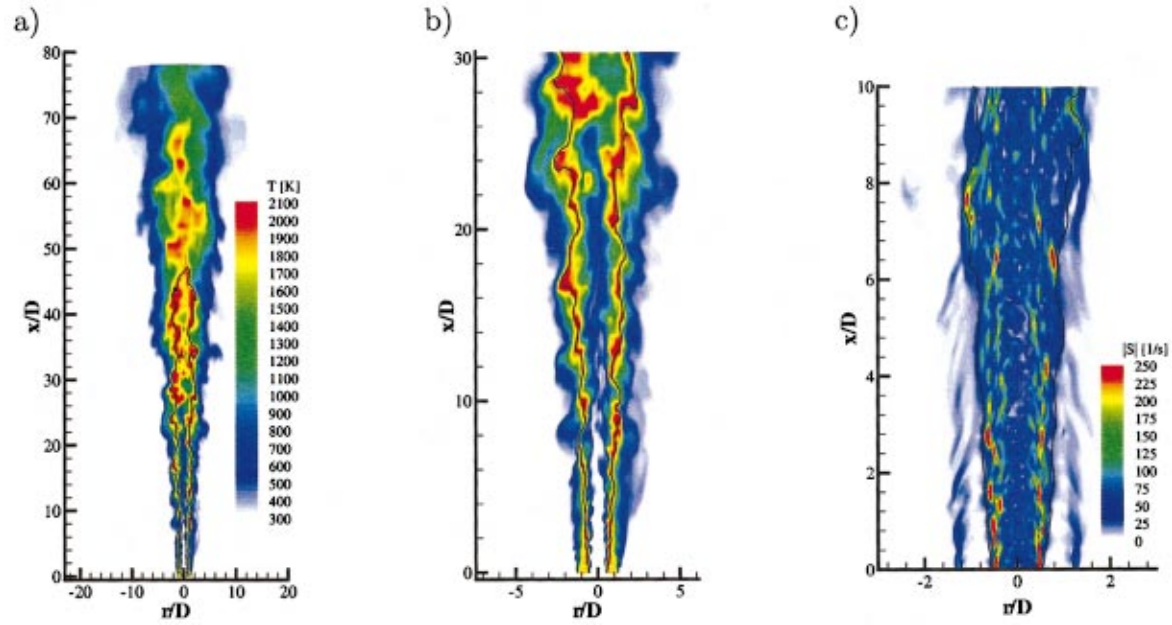

FIG. 6. (Color) Instantaneous temperature and strain rate distribution at a time 3.2 ms later than Fig. 5. The black line represents the contour of a stoichiometric mixture fraction.

note in this figure that close to the nozzle the region around the reaction zone hardly shows turbulent motion and might be regarded as being laminar. This has been found in many experiments and might be of great importance, since for fuels with Lewis numbers different from unity it can be the source of strong differential diffusion effects, which can survive even far downstream of the transition to turbulence as has been discussed in Ref. 20. In order to give an impression of the dynamics of the flame, Figs. 6(a) and 6(b) show the instantaneous temperature distribution at a time approximately 3.2 ms later than in Fig. 5. The comparison with Fig. 5 reveals that the jet core shows a completely different structure, indicating that turbulent structures have been transported far downstream, while in the outer part hardly any motion can be observed. It can also be seen that the location of the flame tip, indicated by the stoichiometric contour can strongly vary with time. For the current calculation the flame tip location moves between approximately $x/D=48$ to $x/D=62$. In order to provide a better picture of the dynamics of the flame, animations of the computational results corresponding to Figs. 5(a) and 5(b) are provided on the world wide web.[49]

The temperature distribution given in Figs. 5 and 6 also allows some qualitative comparison with fundamental observations from experiments in jet diffusion flames. It can be observed, for instance in Fig. 6(b), that regions of very broad high temperature zones around the stoichiometric contour are alternating with regions of very narrow high temperature distribution. In can also be seen that the broad temperature regions always coincide with reaction zones, which are directed outwards, whereas the narrow temperature regions can be associated with reaction zone structures, which are inwardly directed. The analysis shows that these changes are essentially caused by fluctuations in the mixture fraction gradients which also cause fluctuations of the scalar dissipation rate. Since the scalar dissipation rate is also related to the rate of strain, it can be concluded from the calculations that regions of high strain rate are aligned with regions of a narrow temperature maximum. This is in accordance with the experimental findings of Rehm and Clemens.[50] The strain rate field in the region very close to the nozzle is shown in Figs. 5(c) and 6(c). The alignment of the reaction zone and the strain rate field starts to become obvious in the downstream regions of these figures. However, it is interesting to note that closer to the nozzle the reaction zone embraces the region of high rate of strain rather than to follow the high strain layers. This lack of alignment is, as pointed out by Rehm and Clemens,[50] because of the laminar nature of the region around the reaction zone, where the high viscosity does not allow the fluid to freely adjust to the applied strain. Similar structures have been found by Donbar *et al.*[31] in the analysis of two-dimensional CH measurements and PIV measurements in jet diffusion flames. It is generally observed in experiments that these structures occur in an angle with the jet axis of approximately 45°. A similar discussion on the scalar dissipation rate is provided in Ref. 35.

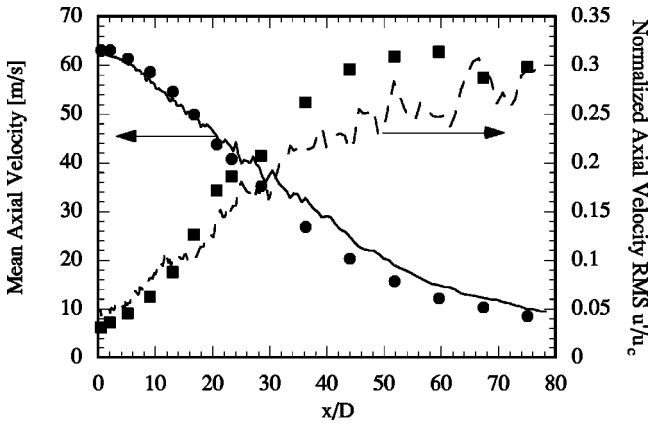

FIG. 7. Mean and RMS of axial velocity along the centerline (lines: calculation; symbols: experiments).

B. Prediction of the flow field

The mean axial velocity and its normalized root mean square (RMS) along the centerline are given in Fig. 7. Both quantities are in reasonable agreement with the experimental data, although the mean values seem to be overpredicted in the far field region of the jet.

Figure 8 shows that the mean mixture fraction is well predicted by the current simulation along the centerline until $x/D=60$. Thereafter, the experimental data is slightly overpredicted. The mixture fraction RMS, including resolved and sub-grid contributions, is also given in Fig. 8. The experiment is slightly underpredicted in the far field of the jet. The underprediction for $x/D<10$ might be attributed to experimental uncertainties, since the RMS has to go to zero close to the nozzle. This conclusion is supported by the comparison of the temperature variance, which will be given in the following. In addition, Fig. 8 shows the sub-grid scale RMS of the mixture fraction, which is shown to be much smaller than the RMS based on the resolved and the sub-grid fluctuations, indicating that the major part of the turbulent mixture fraction fluctuations is resolved by the LES.

Radial mixture fraction profiles are given in Fig. 9 at $x/D=$ 15, 30, and 45. The comparison with the experimental data shows that the general agreement for both the mean and

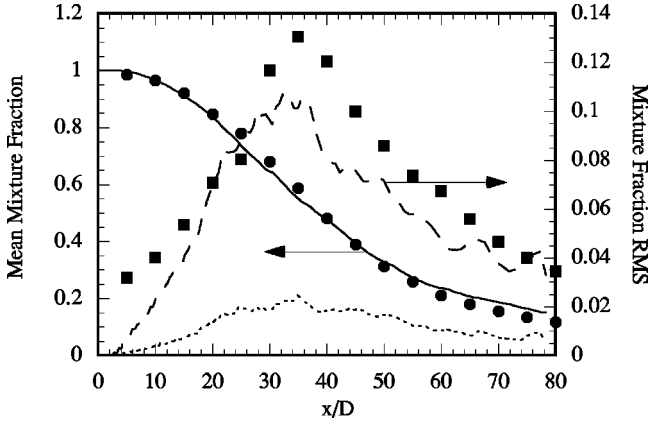

FIG. 8. Mean and RMS of mixture fraction along the centerline (lines: calculation; symbols: experiments).

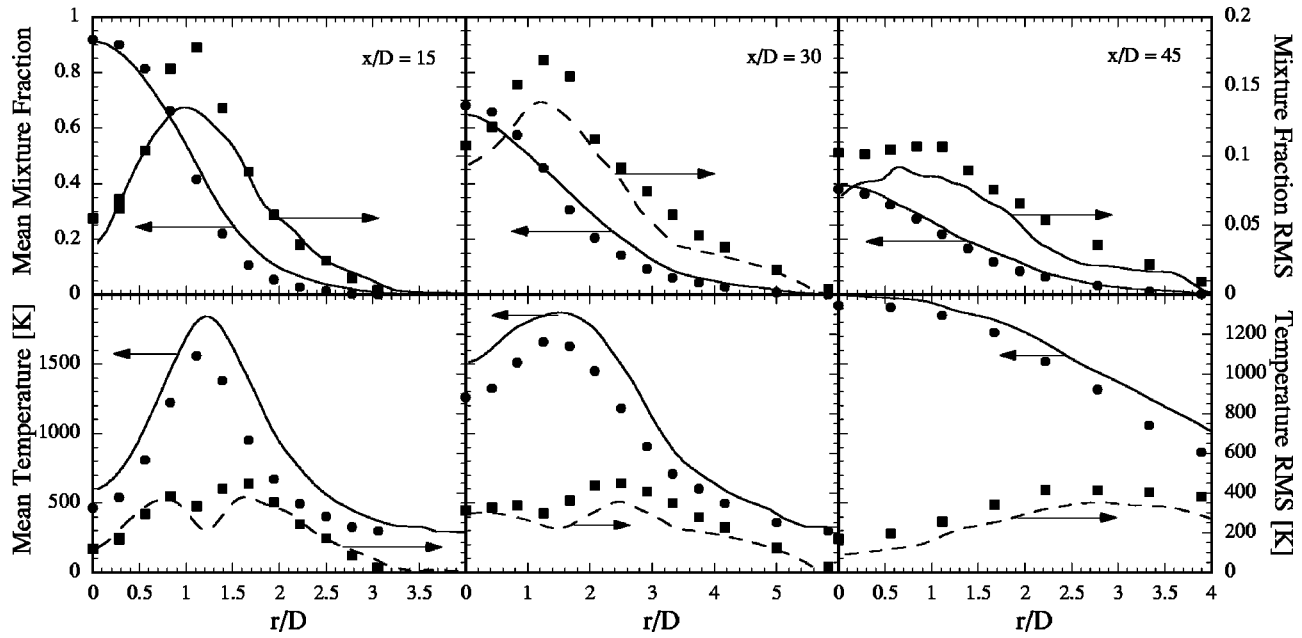

FIG. 9. Radial distribution of mean and the RMS of the mixture fraction and temperature at different downstream positions (lines: calculation; symbols: experiments).

the RMS of the mixture fraction, is reasonable at all these positions, although the maximum values of the mixture fraction RMS seem to be consistently underpredicted.

C. Predictions by the chemistry model

The calculated mean temperature and the temperature RMS along the centerline are shown in Fig. 10. Radial profiles of these quantities are provided in Fig. 9. Both the mean and the RMS agree well with the experimental data. Even the decrease in the temperature RMS around the maximum mean temperature, which can be observed very clearly in the axial profile in Fig. 10, is well represented by the simulation. It is interesting to note that this is not caused by heat release, but is simply because of the vanishing temperature gradient with respect to the mixture fraction. The mean temperature is slightly overpredicted up to $x/D=40$, which will be discussed below.

The following figures show centerline profiles for species mass fractions of CH_4 and O_2 (Fig. 11), H_2O and H_2 (Fig. 12), CO_2 and CO (Fig. 13), and NO and OH (Fig. 14). In general all profiles agree well with the experimental data. Small discrepancies at $x/D>60$ can mainly be attributed to the overprediction of the mixture fraction. In the rich part of the flame at $x/D<40$, H_2O and CO_2 are also slightly overpredicted, while CH_4 and O_2 are underpredicted. Also very obvious is the overprediction of the intermediates H_2 and CO on the rich side. The reason for this is the partial premixing of the fuel with air. As will be shown below, this causes substantial chemical reactions to occur in the rich premixed part of the jet farther downstream. The onset of this partially premixed burning occurs in the current simulation earlier than can be estimated from the experiments. The OH radical

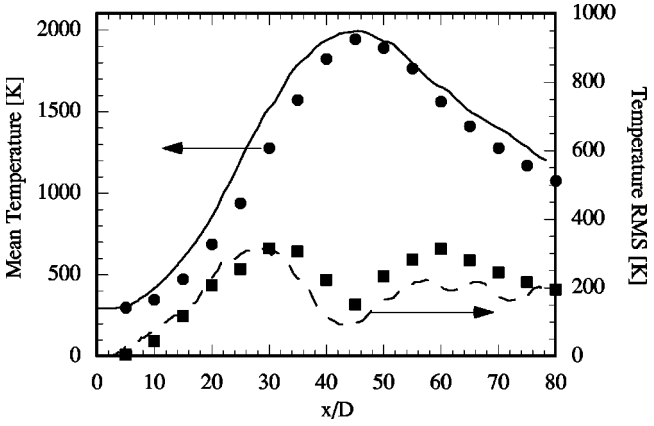

FIG. 10. Mean and RMS of temperature along the centerline (lines: calculation; symbols: experiments).

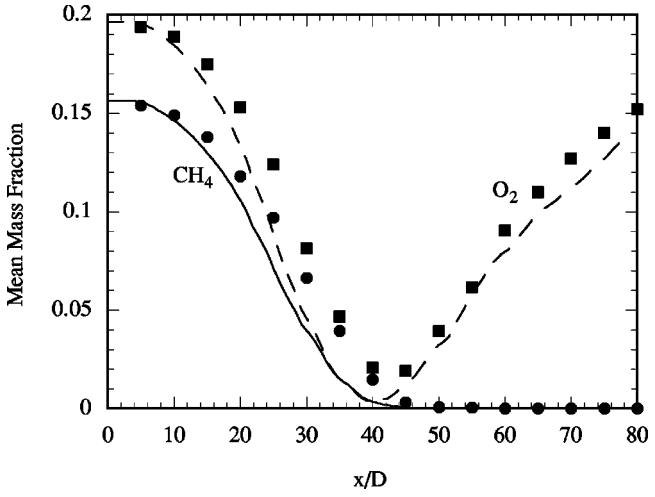

FIG. 11. Mean CH_4 and O_2 mass fractions along the centerline (lines: calculation; symbols: experiments).

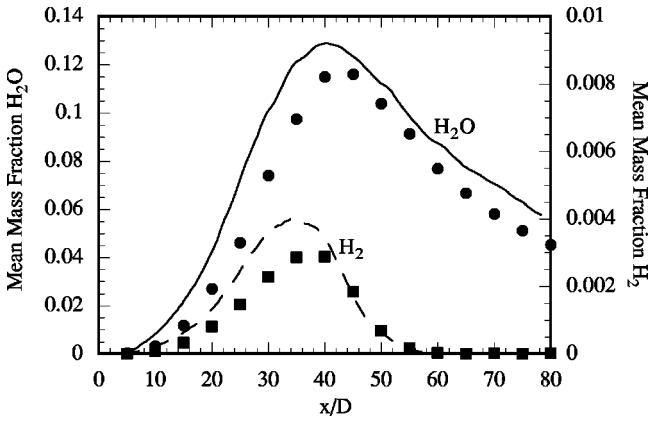

FIG. 12. Mean H_2O and H_2 mass fractions along the centerline (lines: calculation; symbols: experiments).

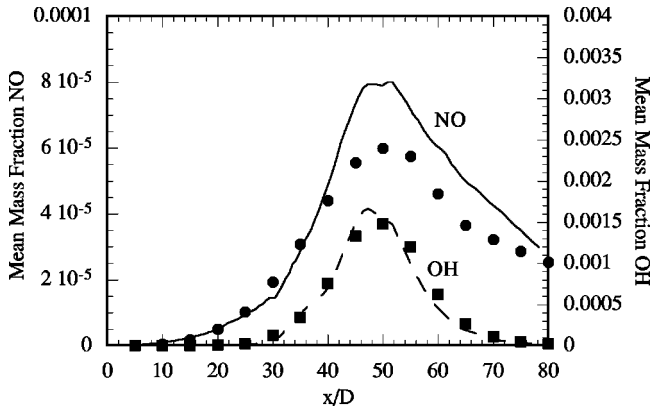

FIG. 14. Mean NO and OH mass fractions along the centerline (lines: calculation; symbols: experiments).

mass fraction shown in Fig. 14 is predicted very accurately. Also the agreement of predicted and measured NO mass fractions can be considered to be very good. The analysis of the formation of nitric oxide shows that only approximately one third of the total NO is formed by the thermal path and that the N_2O path contributes to approximately 10%. The formation of NO is thereby dominated by the prompt path.

The comparison of the radial profiles of the chemical species with the experimental data shows reasonable agreement and does not differ substantially from the centerline profiles. The presentation is therefore being omitted.

Although the results discussed so far are quite encouraging, the conclusions about the chemical structure of the turbulent flame, which can be drawn from these, are quite limited, because only time averaged quantities have been discussed. It is therefore important to compare the time averages of the temperature and mass fractions of the chemical species conditioned on the mixture fraction, because conditioned data provide substantially more insight in turbulence/chemistry interactions.

The conditional averages at the axial locations $x/D=15$, 30, and 45 for the temperature and the mass fractions of the chemical species CH_4, O_2, H_2O, H_2, CO_2, CO, NO, and OH are shown in Fig. 15. At $x/D=15$ the temperature as well as all the species mass fraction profiles agree quite well with the experimental data on the lean side, but tend to overpredict fuel to product conversion on the rich side. In addition to the reasons given above, this can be attributed to the fact that the current model does not allow for local flame extinction. By comparing the simulation with the single point experimental data, it becomes evident that, at least up to a mixture fraction of $Z=0.5$, the temperature, as an example, agrees very well with the burning branch of the data. The lower values of the conditional mean temperature in the experimental data in Fig. 15 are caused by comparably few extinguished data points. This is shown in Fig. 15 for the temperature at $x/D=15$, which includes the single point data from the experiments used to determine the conditional averages. However, this seems to demonstrate the need for an extension of the model.

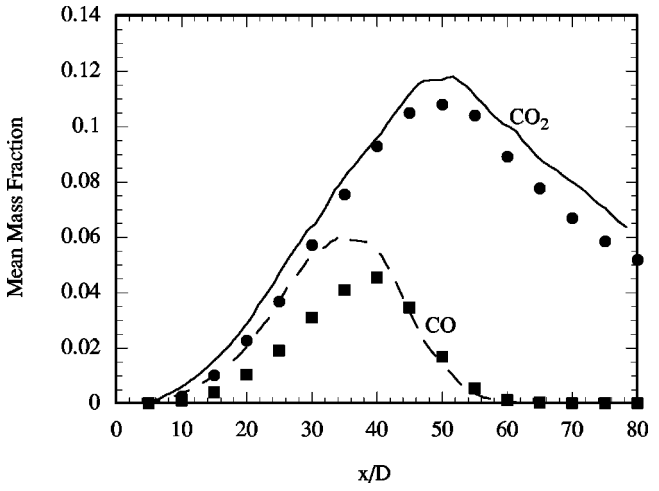

FIG. 13. Mean CO_2 and CO mass fractions along the centerline (lines: calculation; symbols: experiments).

As discussed earlier, the consumption of fuel and molecular oxygen in the fuel consumption layer is slightly overpredicted, which also leads to an overprediction of the water and carbon dioxide values.

Farther downstream at $x/D=30$ the profiles still agree reasonably well with the experimental data. For mixture fraction values of $Z>0.4$ the consumption of CH_4 and O_2 on the rich premixed side is already visible in both the computational results and the experiments. Also, in the predicted and the measured H_2O profile a formation region is observed at approximately $Z=0.6$. However, the partially premixed burning is stronger in the predicted results, which is very obvious in the temperature, and leads to overpredicted intermediate mass fractions. NO is well predicted on the stoichiometric to lean side. However, the predicted profile reveals a NO consumption region at the location of the rich premixed flame, which cannot be observed in the experimental data.

At $x/D=45$ the effect of the partially premixed reaction zone becomes very strong and chemical reactions start at even richer mixtures. This is observed in the temperature profile, which indicates heat release at approximately $Z=0.65$. The partially premixed burning leads to a plateau region in the H_2O profile of the numerical simulation, which is also very obvious in the experiment. Also the CO_2 profile,

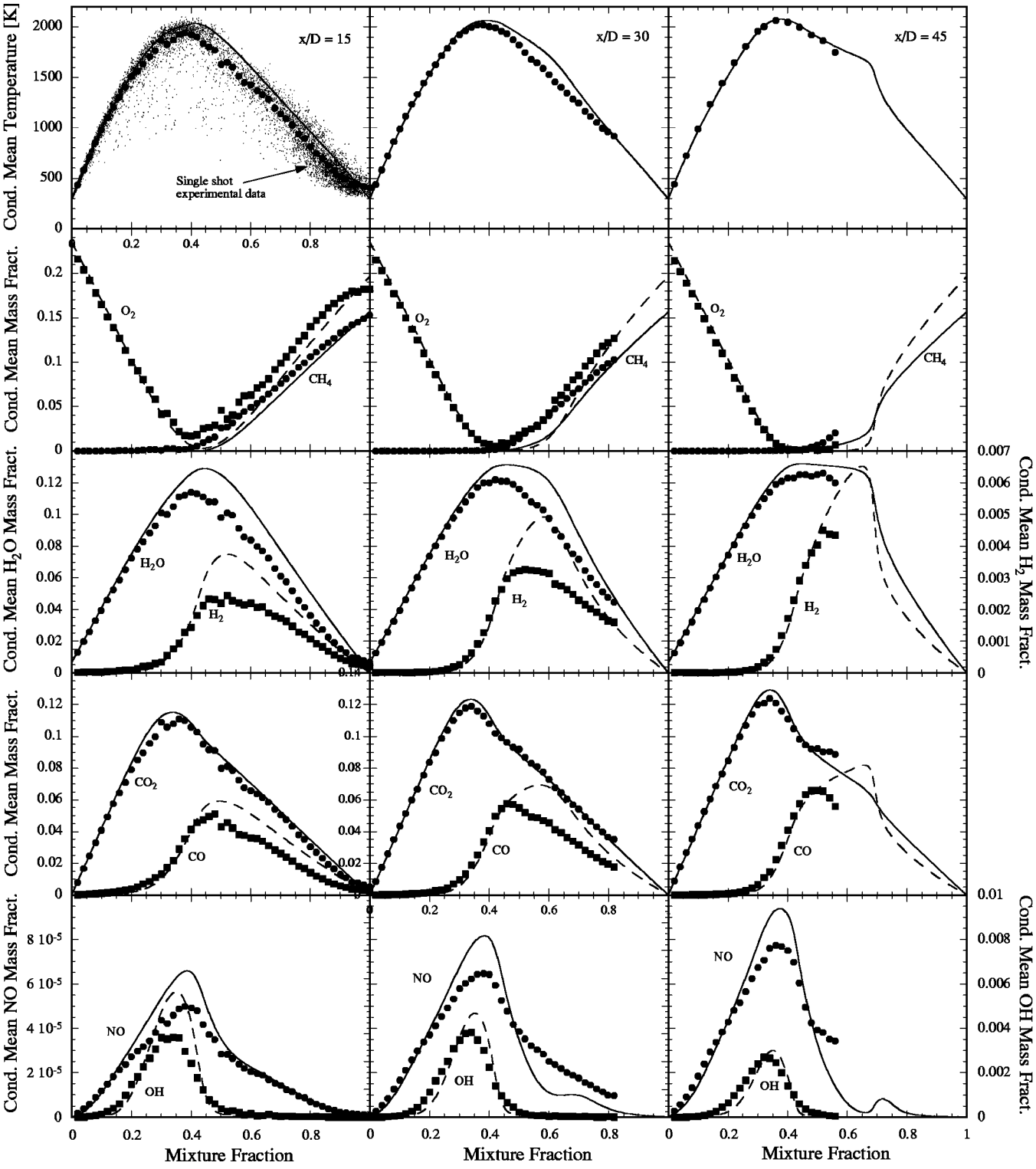

FIG. 15. Conditional averages at different downstream positions (lines: calculation; symbols: experiments).

which is much less influenced by the chemical reactions on the rich side, is in good agreement with the experimental data. The discrepancies discussed for CO and NO on the rich side seem to remain at this location, but are limited to the very rich region. On the lean side the agreement can still be considered to be quite good.

V. CONCLUSIONS

The Lagrangian Flamelet Model, which has been successfully used in RANS calculations of turbulent diffusion flames has been formulated as a combustion model for large-eddy simulations of turbulent jet diffusion flames. The model has been applied in a large-eddy simulation of a turbulent

methane/air flame (Sandia flame D), which has a partially premixed fuel stream. In the LES, sub-grid scale quantities have generally been determined using the Dynamic Procedure. The eddy-diffusivity has been computed from the assumption of a constant sub-grid turbulent Schmidt number. From calculations employing the Dynamic Procedure to compute the eddy diffusivity it has been found that a constant value of $Sc_t = 0.4$ is a very good approximation.

The results are compared with experimental data for the velocity and the mixture fraction field, and for unconditional and conditional averages of temperature and various chemical species, including CO and NO. The agreement is very reasonable for all quantities. The remaining differences have been discussed. In the analysis of the computational results it has been found in accordance with experimental data that regions of high strain appear in layers, which are generally directed inwards. In regions with developed turbulence these layers tend to align with the reaction zone. It has also been found in the analysis of the conditional mean temperature and mass fraction profiles that downstream of $x/D = 30$ chemical reactions lead to substantial fuel consumption in the rich partially part of the flame. In the present calculations the onset of the partially premixed burning occurs to early leading to a slight overprediction in the consumption of the reactants and the formation of water and the intermediates molecular hydrogen and carbon monoxide.

ACKNOWLEDGMENTS

This work was funded in part by the U.S. Department of Energy in the frame of the ASCI program. This support is gratefully acknowledged. The authors are indebted to Robert Barlow for his help in providing the experimental data. We also thank George Kosály for many helpful discussions.

[1] P. E. DesJardin and S. H. Frankel, ''Large eddy simulation of a nonpremixed reacting jet: Application and assessment of subgrid-scale combustion models,'' Phys. Fluids **10**, 2298 (1998).
[2] S. M. De Bruyn Kops, J. J. Riley, G. Kolaly, and A. W. Cook, ''Investigation of modeling for non-premixed turbulent combustion,'' Flow, Turbul. Combust. **60**, 105 (1998).
[3] A. W. Cook and J. J. Riley, ''A subgrid model for equilibrium chemistry in turbulent flows,'' Phys. Fluids **6**, 2868 (1994).
[4] A. W. Cook, J. J. Riley, and G. Kosaly, ''A laminar flamelet approach to subgrid-scale chemistry in turbulent flows,'' Combust. Flame **109**, 332 (1997).
[5] A. W. Cook and J. J. Riley, ''Subgrid-scale modeling for turbulent reactive flows,'' Combust. Flame **112**, 593 (1998).
[6] W. K. Bushe and H. Steiner, ''Conditional moment closure for large eddy simulation of nonpremixed turbulent reacting flows,'' Phys. Fluids **11**, 1896 (1999).
[7] P. J. Colucci, F. A. Jaberi, P. Givi, and S. B. Pope, ''Filtered density function for large eddy simulation of turbulent reacting flows,'' Phys. Fluids **10**, 499 (1998).
[8] A. R. Kerstein, ''A linear-eddy model of turbulent scalar transport and mixing,'' Combust. Sci. Technol. **60**, 391 (1988).
[9] P. A. McMurtry, S. Menon, and A. R. Kerstein, ''A linear eddy sub-grid model for turbulent reacting flows: Application to hydrogen-air combustion,'' Proc. Combust. Inst. **24**, 271 (1992).
[10] S. B. Pope, ''Pdf methods for turbulent reactive flows,'' Prog. Energy Combust. Sci. **11**, 119 (1985).
[11] J. Y. Chen, W. Kollman, and R. W. Dibble, ''Pdf modeling of turbulent methane–air nonpremixed jet flames,'' Combust. Sci. Technol. **64**, 315 (1989).
[12] V. Saxena and S. B. Pope, ''Pdf calculations of major and minor species in a turbulent poloted jet flame,'' Proc. Combust. Inst. **27**, 1081 (1998).
[13] F. Gao and E. E. O'Brien, ''A large-eddy simulation scheme for turbulent reacting flows,'' Phys. Fluids A **5**, 1282 (1993).
[14] J. Jimenez, A. Linan, M. M. Rogers, and F. J. Higuera, ''*A priori* testing of subgrid models for chemically reacting non-premixed turbulent shear flows,'' J. Fluid Mech. **349**, 149 (1997).
[15] C. K. Madnia and P. Givi, ''Direct numerical simulation and large eddy simulation of reacting homogeneous turbulence,'' in *Large Eddy Simulation of Complex Engineering and Geophysical Flows*, edited by B. Galperin and S. A. Orszag (Cambridge University Press, Cambridge, 1993).
[16] C. Wall, B. Boersma, and P. Moin, ''An evaluation of the assumed beta probability density function subgrid-scale model for large eddy simulation of nonpremixed, turbulent combustion with heat release,'' Phys. Fluids **7**, 2522 (2000).
[17] C. D. Pierce and P. Moin, ''A dynamic model for subgrid-scale variance and dissipation rate of a conserved scalar,'' Phys. Fluids **10**, 3041 (1998).
[18] H. Steiner and W. K. Bushe, ''Large eddy simulation of a turbulent diffusion flame with conditional source-term estimation,'' Phys. Fluids (submitted).
[19] H. Pitsch, M. Chen, and N. Peters, ''Unsteady flamelet modeling of turbulent hydrogen/air diffusion flames,'' Proc. Combust. Inst. **27**, 1057 (1998).
[20] H. Pitsch, ''Unsteady flamelet modeling of differential diffusion in turbulent jet diffusion flames,'' Combust. Flame (accepted).
[21] R. S. Barlow and J. H. Frank, ''Effect of turbulence on species mass fractions in methane/air jet flames,'' Proc. Combust. Inst. **27**, 1087 (1998).
[22] R. S. Barlow and J. Frank, www.ca.sandia.gov/tdf/Workshop.html, 1998.
[23] E. Hassel, www.ca.sandia.gov/tdf/Workshop.html, 1998.
[24] P. Moin, K. Squires, W. Cabot, and S. Lee, ''A dynamic subgrid-scale model for compressible turbulence and scalar transport,'' Phys. Fluids A **3**, 2746 (1991).
[25] N. Peters, ''Laminar diffusion flamelet models in non-premixed turbulent combustion,'' Prog. Energy Combust. Sci. **10**, 319 (1984).
[26] N. Peters, ''Laminar flamelet concepts in turbulent combustion,'' Proc. Combust. Inst. **21**, 1231 (1987).
[27] H. Pitsch and N. Peters, ''A consistent flamelet formulation for non-premixed combustion considering differential diffusion effects,'' Combust. Flame **114**, 26 (1998).
[28] N. Smith, J. Gore, and J. Kim, http://www.ca.sandia.gov/tdf/Workshop/Submodels.html, 1998.
[29] C. H. Gibson, ''Fine structure of scalar fields mixed ty turbulence. I. Zero-gradient points and minimal gradient surfaces,'' Phys. Fluids **11**, 2305 (1968).
[30] N. Peters, *Turbulent Combustion* (Cambridge University Press, Cambridge, 2000).
[31] J. M. Donbar, J. F. Driscoll, and D. C. Carter, ''Strain rates measured along the wrinkled flame contour within turbulent nonpremixed jet flames,'' presented at the Joint Meeting of the U.S. Sections of the Combustion Institute, Washington, DC, 1999.
[32] S. S. Girimaji and Y. Zhou, ''Analysis and modeling of subgrid scalar mixing using numerical data,'' Phys. Fluids **8**, 1224 (1996).
[33] M. D. Smooke and V. Giovangigli, ''Formulation of the premixed and nonpremixed test problems,'' in *Reduced Kinetic Mechanisms and Asymptotic Approximations for Methane-Air Flames*, edited by M. D. Smooke (Springer Verlag, Berlin, 1991).
[34] J. S. Kim and F. A. Williams, ''Structures of flow and mixture-fraction fields for counter-flow diffusion flames with small stoichiometric mixture fractions,'' SIAM (Soc. Ind. Appl. Math.) J. Appl. Math. **53**, 1551 (1993).
[35] H. Pitsch and H. Steiner, ''Scalar mixing and dissipation rate in large-eddy simulations of non-premixed turbulent combustion,'' Proc. Combust. Inst. (accepted).
[36] V. R. Kuznetsov and V. A. Sabel'nikov, *Turbulence and Combustion* (Hemisphere, New York, 1990).
[37] B. J. Boersma, G. Brethouwer, and F. T. M. Nieuwstadt, ''A numerical investigation on the effect of the inflow conditions on the self-similar region of a round jet,'' Phys. Fluids **10**, 899 (1998).
[38] H. N. Najm, P. S. Wyckoff, and O. M. Knio, ''A semi-implicit numerical scheme for reacting flow,'' J. Comput. Phys. **143**, 381 (1998).
[39] I. Danaila and B. J. Boersma, ''DNS of forced jet at low Reynolds numbers, in *Proceedings of the 1998 Summer Program*, Center for Turbulence Research, NASA Ames/Stanford University, 1998, p. 141.
[40] K. Akselvoll and P. Moin, ''Large-eddy simulation of turbulent confined coannular jets,'' J. Fluid Mech. **315**, 387 (1996).

[41]P. M. Gresho, ''Incompressible fluid dynamics: Some fundamental formulations issues,'' Annu. Rev. Fluid Mech. **23**, 413 (1991).
[42]H. Pitsch, ''A C++ computer program for 0-D combustion and 1-D laminar flame calculations,'' RWTH Aachen, 1998.
[43]C. T. Bowman, R. K. Hanson, D. F. Davidson *et al.*, Gri-mech 2.11, http://www.me.berkeley.edu/gri_mech/.
[44]G. P. Smith, D. M. Golden, M. Frenklach, N. W. Moriarty, B. Eiteneer, M. Goldenberg, C. T. Bowman, R. Hanson, S. Song, W. C. Gardiner, Jr., V. Lissianski, and Z. Qin, Gri-mech 3.0, http://www.me.berkeley.edu/gri_mech/.
[45]N. Peters, ''Flame calculations with reduced mechanisms—an outline,'' in *Reduced Kinetic Mechanisms for Applications in Combustion Systems*, edited by N. Peters and B. Rogg (Springer-Verlag, Berlin, 1993).
[46]S. C. Li and F. A. Williams (private communication, 1999).
[47]J. Warnatz, U. Maas, and R. W. Dibble, *Combustion, Physical and Chemical Fundamentals, Modeling and Simulation, Experiments, Pollutant Formation* (Springer-Verlag, New York, 1996).
[48]H. Wang, A. Laskin, Z. M. Djurisic, C. K. Law, S. G. Davis, and D. Zhu, ''A comprehensive mechanism of C_2H_x and C_3H_x fuel combustion,'' presented at the Fall Technical Meeting of the Eastern States Section of the Combustion Institute, Raleigh, 1999.
[49]H. Pitsch, www.stanford.edu/~hpitsch.
[50]J. E. Rehm and N. T. Clemens, ''The relationship between vorticity/strain and reaction zone structure in turbulent non-premixed jet flames,'' Proc. Combust. Inst. **27**, 1113 (1998).